Technische Universität Graz

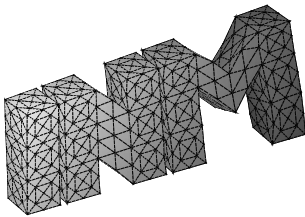# On the influence of the wall shear stress vector form on hemodynamic indicators

L. John, P. Pustejovska, O. Steinbach

**Berichte aus dem
Institut für Numerische Mathematik**

Technische Universität Graz

On the influence of the wall shear stress vector form
on hemodynamic indicators

L. John, P. Pustejovska, O. Steinbach

Berichte aus dem
Institut für Numerische Mathematik

Technische Universität Graz
Institut für Numerische Mathematik
Steyrergasse 30
A 8010 Graz

WWW: `http://www.numerik.math.tu-graz.at`

On the influence of the wall shear stress vector form on hemodynamic indicators

L. John[1], P. Pustějovská[1], O. Steinbach[1]

[1] Institute of Computational Mathematics,
Graz University of Technology,
Steyrergasse 30,
A-8010 Graz, Austria

`{john,pustejovska,o.steinbach}@tugraz.at`

Abstract

Hemodynamic indicators such as the averaged wall shear stress (AWSS) and the oscillatory shear index (OSI) are well established to characterize areas of arterial walls with respect to the formation and progression of aneurysms. Here, we study two different forms for the wall shear stress vector from which AWSS and OSI are computed. One is commonly used as a generalization from the two-dimensional setting, the latter is derived from the full decomposition of the wall traction force given by the Cauchy stress tensor. We compare the influence of both approaches on hemodynamic indicators by numerical simulations under different computational settings. Namely, different (real and artificial) vessel geometries, and the influence of a physiological periodic inflow profile. The blood is modeled either as a Newtonian fluid or as a generalized Newtonian fluid with a shear rate dependent viscosity. Numerical results are obtained by using a stabilized finite element method. We observe profound differences in hemodynamic indicators computed by these two approaches, mainly at critical areas of the arterial wall.

Keywords: Blood flow; wall shear stress; oscillatory shear index; aneurysm; generalized Newtonian model; stabilized finite element method.

1 Introduction

In this article, we aim to analyze the influence of different computational settings on the blood flow dynamics, with a focus on the identification of the main hemodynamic indicators in application to the aneurysm problematics. For that, we shall consider different computational geometries, both real and artificial, different inflow conditions and hemodynamic

models, and mainly, different approaches for computing the shear stresses at the arterial walls. We shall not discuss the influence of the mechanical interaction between the vessel wall and the blood, in order to characterize the main properties of the above mentioned setups. This should be nevertheless considered in a following work.

Even though blood is a mixture of biological substances (namely blood cells suspended in a blood plasma medium consisting of water, macromolecules and ions), we consider it, on the macroscopic scale, as a single constituent incompressible, homogeneous and isotropic fluid. Thus, we shall describe its flow in the framework of continuum mechanics. In such a case, the fluid model is given by the Cauchy stress tensor

$$\boldsymbol{T} = -p\boldsymbol{I} + \boldsymbol{S}, \tag{1.1}$$

where $p\boldsymbol{I}$ is the mean normal stress (with p denoting the hydrodynamical pressure) and $\boldsymbol{S}$ is the extra stress tensor which needs to be specified by a suitable constitutive equation reflecting the rheological nature of the considered fluid.

For the needs of computational simplicity, blood is very commonly considered as a Newtonian fluid, that means, its rheological behavior is described by a single parameter, called viscosity, being a constant of proportionality between the shear stress and the shear rate during a simple shear. Such an approximation can be validated for blood flow in vessels with large diameters. This, on the other hand, should not be presumed in the case of blood flow in a vessel with aneurysm where its typical non-Newtonian phenomena occur. Moreover, the focus of this work is laid on the identification of the distribution of the wall shear stresses, and thus, a Newtonian description of blood can significantly influence the relevancy of an aimed computational prediction.

1.1 Hemodynamic models

In a physiological environment, the non-Newtonian character of blood manifests in its ability to thin the shear and the stress relaxation. The shear-thinning behavior and its connection to the red blood cell (RBCs) deformation and rouleau aggregation was originally recognized already in the 1970's in the work of Chien et al.[4, 5]. Shortly after, Thurston in [22] described the property of RBCs to store energy via the rouleau network deformation and consequently measured the viscoelastic nature of the whole blood. Such a behavior, related to the rouleau network deformation, must be thus shear-rate dependent as it is the formation of such a structure, see [23]. Surprisingly, until now, only few viscoelastic models (describing among others the mentioned stress relaxation) have been proposed: a linear Maxwell model proposed by Thurston [22], a generalized Oldroyd-B model with a non-linear apparent viscosity of shear-thinning proposed by Yeleswarapu et al.[26], and recently, a thermodynamically consistent model of Anand and Rajagopal [1] describing blood as a mixture of shear-thinning viscoelastic and Newtonian fluid, created in the framework of maximization of the rate of dissipation corresponding to the material natural (stress-free) configuration.

For our aim, we assume standard Newtonian model given by

$$\boldsymbol{S} = 2\mu\boldsymbol{D}, \tag{1.2}$$

where $\boldsymbol{D}$ is the symmetric part of the velocity gradient, that means $\boldsymbol{D} = \frac{1}{2}(\nabla\boldsymbol{u} + \nabla\boldsymbol{u}^{\top})$, and μ denotes the constant dynamic viscosity. As a second model, we shall consider a generalized Newtonian model describing the shear-thinning property of blood, namely

$$\boldsymbol{S} = 2\mu(|\boldsymbol{D}|^2)\boldsymbol{D}, \tag{1.3}$$

where the generalized viscosity μ is shear rate dependent, having the form of a power-law-like Carreau[1] model, see [7, Part II],

$$\mu(|\boldsymbol{D}|^2) = \eta_\infty + (\eta_0 - \eta_\infty)(1 + \kappa|\boldsymbol{D}|^2)^n. \tag{1.4}$$

Here η_0, η_∞, κ and n are material parameters. While $\kappa > 0$ and $n \in (-0.5, 0)$ are parameters of shear-thinning, η_0 and η_∞ are asymptotic apparent viscosities of blood for the shear rates $\dot{\gamma} \to 0$ and $\dot{\gamma} \to \infty$, respectively. From this, it is clear that η_0, η_∞ are (in theory) independent of the particular shear-thinning model, while κ and n need to be specified from the specific model that they fit the experimental data. In this work, we use the values[2] of material parameters as given in [7, Chapter II], namely $\eta_0 = 65.7 \times 10^{-3}$ Pa s, $\eta_\infty = 4.45 \times 10^{-3}$ Pa s, $\kappa = 212.2$ s^2, and $n = -0.325$. In the case of the Newtonian model we use $\mu = \eta_\infty$.

As one can see, we completely neglect possible pathological influences on the blood rheology which can occur in the case of blood flow in aneurysm sack, like degeneration of the blood cells, thrombus formation etc., see for instance [21]. Nevertheless, such biochemical questions should be discussed, and in order of a better description of the blood flow nature in aneurysm, more advanced hemodynamic models with biochemical part should be considered. On the other hand, as it was mentioned above, we focus mainly on the description of the effects of real geometries and flow conditions on the wall shear stresses, and thus a generalized Newtonian shear-thinning model can be considered as a reasonable approximation. A consideration of more rigorous models of blood can be seen as a future work.

1.2 Equations of flow and their non-dimensionalization

We describe the flow of blood in terms of the velocity field $\boldsymbol{u}(t, x)$ and the pressure $p(t, x)$ which are governed by the non-stationary incompressible (generalized) Navier–Stokes equations with different viscosity models as given in (1.2) and (1.4). For the consecutive

---

[1]It is very common that the shear-thinning of blood is described by a more general Carreau–Yasuda model, having in comparison with the Carreau model one more additional material parameter. Nevertheless, in the case of blood, both models give the same quantitative and qualitative fits. Thus we use the simpler one.

[2]In general, blood viscosity is depending on many factors like hematocrit, pH, age, gender, etc., and thus different values of fitted material parameters can be found through the literature.

numerical computations, it will be useful to recast the governing equations in terms of dimensionless variables, defined as follows

$$X = \frac{x}{L^*}, \quad \boldsymbol{U} = \frac{\boldsymbol{u}}{U^*}, \quad P = \frac{p}{P^*}, \quad M = \frac{\mu}{M^*}, \tag{1.5}$$

where L^* and U^* are the characteristic length and velocity, respectively, M^* is the characteristic dynamic viscosity and P^* is the scaling pressure. All the $*$-characteristic values are suitably chosen for a particular computational setting in order to describe the character of the specific flow problem. For consistency, we choose

$$P^* = \varrho(U^*)^2 \quad \text{and} \quad M^* = \eta_\infty, \tag{1.6}$$

where ϱ is the density of the fluid. Then the time is naturally non-dimensionalized with respect to L^*/U^* and the same holds true for the extra stress tensor $\boldsymbol{S}$ with respect to M^*U^*/L^*.

For simplicity of the notation, instead of capitals, small letters for the non-dimensional variables are used. The system of governing equations is then transformed onto

$$\frac{\partial \boldsymbol{u}}{\partial t} + [\nabla \boldsymbol{u}]\boldsymbol{u} = -\nabla p + \frac{2}{\text{Re}} \, \text{div}\left(\mu(|\boldsymbol{D}|^2)\boldsymbol{D}\right), \tag{1.7}$$

$$\text{div} \, \boldsymbol{u} = 0, \tag{1.8}$$

using the notation for the reduced Reynolds number[3] $\text{Re} = \varrho L^* U^*/\mu_\infty$. In the case of a Newtonian fluid we have then $\mu(\cdot) = 1$.

2 Hemodynamic indicators

The initiation, evolution and rupture of aneurysm result, as most degenerative cardiovascular diseases, from a combination of hemodynamics, vessel wall mechanics, and physical and biochemical processes within and between them. In the past decades, the hypothesis of strong correlation between the blood flow induced mechanical stresses and the arterial wall functionality, degenerative chemical processes within and around it has been several times verified [6, 10, 11, 13, 15, 17, 19, 25]. More precisely, the endothelial cells of the vessel wall are mechanosensitive to the local shear stresses [14, 25], transferring the abnormal wall shear stress into specific biochemical signals which modulate the cellular structure of the wall. This results in the wall thinning [10] and in an increase of the lipid and adhesion molecules permeability through the wall [6], which is connected to aneurysm plaque or thrombus formation. On the other hand, the physiological level of the shear stress at the wall is protective. As specified for example in [14], the range[4] of wall shear stress is about

---

[3]Sometimes, the Navier–Stokes equations are expressed in terms of the kinematic viscosity $\nu = \mu/\rho$. Nevertheless, in the case of non-dimensionalization, this issue is irrelevant due to the Reynolds number being then of the form $\text{Re} = L^*U^*/\nu$.

[4]The range in non-dimensionalized physical quantities shall be specified later.

$15 - 70$ dyne cm^{-2}. From above it is clear that identification of local wall shear stress (WSS) plays an important role in the study of aneurysm evolution *in silico*, and thus, it shall be a key factor in the characterization of aneurysm in this work.

Across the literature one can find different approaches to the WSS computation. By a rheological definition, WSS is a shear traction caused by the blood flow acting on the endothelial cell surface. In terms of the Cauchy stress tensor this means

$$\text{WSS} \coloneqq (\boldsymbol{Tn}) \cdot \boldsymbol{t}_{\text{blood}}, \tag{2.1}$$

where $\boldsymbol{n}$ is the outer normal unit vector of the tangential plane to the vessel wall. Then $\boldsymbol{t}_{\text{blood}}$ is a tangential unit vector living in such a plane, having the same direction as the velocity vector of blood. Notice, that $(\boldsymbol{Tn}) \cdot \boldsymbol{t}_{\text{blood}}$ is in our problem always non-negative. For a two-dimensional case of unidirectional flow, this characterization is intuitive due to the unique identification of $\boldsymbol{t}_{\text{blood}}$. Similarly, such characterization of wall shear stress is meaningful also for simple shear flow in three-dimensional case. Let us be more concrete and derive WSS for simple shear flow described in Cartesian coordinates in the x-axis. Then, the velocity vector and the corresponding normal and tangential unit vectors are

$$\boldsymbol{v} = (v_1(y), 0, 0)^\top, \quad \boldsymbol{n} = (0, 1, 0)^\top, \quad \boldsymbol{t}_{\text{blood}} = (1, 0, 0)^\top. \tag{2.2}$$

Correspondingly we have

$$(\boldsymbol{Tn}) \cdot \boldsymbol{t}_{\text{blood}} = -p\,\boldsymbol{n} \cdot \boldsymbol{t}_{\text{blood}} + 2\mu(\cdot)\boldsymbol{Dn} \cdot \boldsymbol{t}_{\text{blood}} \tag{2.3}$$

$$= \mu(\cdot) \begin{pmatrix} 0 & \frac{\partial v_1(y)}{\partial y} & 0 \\ \frac{\partial v_1(y)}{\partial y} & 0 & 0 \\ 0 & 0 & 0 \end{pmatrix} \begin{pmatrix} 0 \\ 1 \\ 0 \end{pmatrix} \cdot \begin{pmatrix} 1 \\ 0 \\ 0 \end{pmatrix} = \mu(\cdot)\frac{\partial v_1(y)}{\partial y}. \tag{2.4}$$

Obviously, for simple shear flow for which the flow is purely laminar, the wall shear stress vector and the (scalar) wall shear stress are then derived as

$$\boldsymbol{\tau}_{w,1} = 2\mu(\cdot)\boldsymbol{Dn}, \qquad \text{WSS}_1 = |2\mu(\cdot)\boldsymbol{Dn}|. \tag{2.5}$$

Such a derivation then tempt, that these formulas are also used in general three-dimensional setting, see for example [9, 12, 13, 14, 20]. However, for complicated geometries, like the arteries with aneurysms, the flow at the arterial wall can not be approximated by simple shear, since a non-negligible part of $\boldsymbol{Dn}$ will not act in the shear direction. Formula (2.1) is then for those problems not usable, since $\boldsymbol{t}_{\text{blood}}$ is given by two a priori not known tangential vectors, and thus, together with zero Dirichlet boundary condition for the velocity one can not directly derive it in this way.

Instead, one can use a full decomposition approach. The shear stress vector is then derived from the wall traction $\boldsymbol{Tn}$ by subtracting the normal stress vector as depicted in Fig. 2.1. That means

$$\boldsymbol{\tau}_{w,2} = \boldsymbol{Tn} - [(\boldsymbol{Tn}) \cdot \boldsymbol{n}]\boldsymbol{n} \tag{2.6}$$

$$= -p\boldsymbol{n} + \boldsymbol{Sn} + [(p\boldsymbol{n} \cdot \boldsymbol{n})]\boldsymbol{n} - [(\boldsymbol{Sn}) \cdot \boldsymbol{n}]\boldsymbol{n} \tag{2.7}$$

$$= \boldsymbol{Sn} - [(\boldsymbol{Sn}) \cdot \boldsymbol{n}]\boldsymbol{n}, \tag{2.8}$$
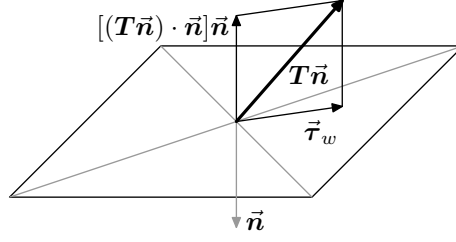
Figure 2.1: Stress decomposition at the infinitesimal plane into its normal and tangential part. In the case that $\boldsymbol{n}$ coincides with the outer normal of the vessel wall, we call the tangential part $\boldsymbol{\tau}_w$ the wall shear stress vector.

and specifically for the (generalized) Newtonian case

$$\boldsymbol{\tau}_{w,2} = \boldsymbol{T}\boldsymbol{n} - [(\boldsymbol{T}\boldsymbol{n}) \cdot \boldsymbol{n}]\boldsymbol{n} \tag{2.9}$$
$$= 2\mu(\cdot)(\boldsymbol{D}\boldsymbol{n} - [(\boldsymbol{D}\boldsymbol{n}) \cdot \boldsymbol{n}]\boldsymbol{n}). \tag{2.10}$$

By the uniqueness of the decomposition of a traction vector into its normal and shear part, we obtain

$$\mathrm{WSS}_2 = |\boldsymbol{\tau}_{w,2}|. \tag{2.11}$$

Here one should notice that the normal stress is not identified with the mean normal stress $[-p\boldsymbol{I}]\boldsymbol{n}$ but it is superposed together with $[(\boldsymbol{S}\boldsymbol{n}) \cdot \boldsymbol{n}]\boldsymbol{n}$. This normal part of the extra stress is very often neglected, reasoned by the flow conditions close to the simple shear. Later we shall see that this term is nevertheless not of small order mainly at the critical points of the domain where aneurysm or arterial plaque appear.

Whatever definition of WSS we use, it is still a local physical quantity expressed at a given time. Thus, it is preferable to consider this indicator over a certain time period, either the time of observation or the period of the cardiac cycle. For this, we introduce a time-averaged wall shear stress (AWSS) as proposed in [13], characterizing the areas of low shear stresses at the vessel wall during the time interval $(0, T)$

$$\mathrm{AWSS} := \frac{1}{T} \int_0^T |\boldsymbol{\tau}_w(t)| \, dt, \tag{2.12}$$

where $\boldsymbol{\tau}_w$ is the wall shear stress vector. Thus, as we are interested in the differences arising from the choice of the form of $\boldsymbol{\tau}_w$, we define

$$\mathrm{AWSS}_1 := \frac{1}{T} \int_0^T |\boldsymbol{\tau}_{w,1}(t)| \, dt, \quad \mathrm{AWSS}_2 := \frac{1}{T} \int_0^T |\boldsymbol{\tau}_{w,2}(t)| \, dt. \tag{2.13}$$

However, in the case of a pulsative flow, some pathological flow patterns at or near the wall can develop, such as stagnation points or wall shear stresses with oscillating character, for which a quantity such as AWSS can be high as well. This is due to the fact that AWSS

is computed from the magnitude of the shear force and thus it is free from the information about the oscillatory character. Hence we introduce, see [13], an additional hemodynamic indicator, the oscillatory shear index (OSI)

$$\text{OSI} := \frac{1}{2} \left(1 - \frac{\left| \int_0^T \boldsymbol{\tau}_w(t) \, dt \right|}{\int_0^T |\boldsymbol{\tau}_w(t)| \, dt} \right), \tag{2.14}$$

to provide a characterization of the deviation of the WSS vector from its averaged direction, in other words a measure of WSS oscillations where AWSS is not predictive. Here, $\int_0^T \boldsymbol{a}(t) \, dt$ stands for a vector with components computed as integrals of corresponding components of the vector $\boldsymbol{a}$. In the case that the denominator in (2.14) is zero, we set $\text{OSI} = 0$, since in that case the nominator adopts zero value as well. The values of OSI are in the range $[0, 0.5]$, where $\text{OSI} = 0$ corresponds to a unidirectional flow (protective) and $\text{OSI} = 0.5$ to a purely oscillating flow (pathological). Again, in the same fashion as (2.13), we define

$$\text{OSI}_1 := \frac{1}{2} \left(1 - \frac{\left| \int_0^T \boldsymbol{\tau}_{w,1}(t) \, dt \right|}{\int_0^T |\boldsymbol{\tau}_{w,1}(t)| \, dt} \right), \quad \text{OSI}_2 := \frac{1}{2} \left(1 - \frac{\left| \int_0^T \boldsymbol{\tau}_{w,2}(t) \, dt \right|}{\int_0^T |\boldsymbol{\tau}_{w,2}(t)| \, dt} \right). \tag{2.15}$$

From what has been described above, both indicators need to be investigated simultaneously, with a focus on the regions where either AWSS and OSI are small, or, OSI is high regardless of the AWSS value.

3 Computational setup

3.1 Geometry and data

We consider four different geometries of cerebral arteries with aneurysm, three realistic, reconstructed from CTA imaging, and one artificial (symmetric), see Fig. 3.1. Geometry GEOM_1 was obtained as open source mesh from the CISTIB lab at the Universitat Pompeu Fabra of Barcelona, GEOM_2 was provided from [8], and GEOM_3 from [16].

We always denote the domain of interest by Ω and its boundary by Γ which is decomposed into three parts, namely the boundary of the wall and the parts of inflow and outflow, i.e. $\overline{\Gamma} = \overline{\Gamma}_w \cup \overline{\Gamma}_{in} \cup \overline{\Gamma}_{out}$, all of positive measure.

Under normal conditions, the diameter of a cerebral artery is approximately $5 \, \text{mm}$, and, as it will be specified below, the velocity inflow is in the range $10 - 50 \, \text{cm s}^{-1}$. This, together with the viscosity $\eta_\infty = 4.45 \times 10^{-3} \, \text{Pa s}$, gives us the characteristic units of the problem under consideration,

$$L^* = 1 \, \text{cm}, \quad U^* = 10 \, \text{cm s}^{-1}, \quad \frac{M^*}{\varrho} = 4.2 \times 10^{-2} \, \text{cm}^2 \text{s}^{-1}, \tag{3.1}$$

which scales the time by $T^* = 0.1 \, \text{s}$ and the stress by $S^* = 0.445 \, \text{dynes cm}^{-2}$. The corresponding Reynolds number is then $\text{Re} \approx 240$. The mesh geometries are scaled into

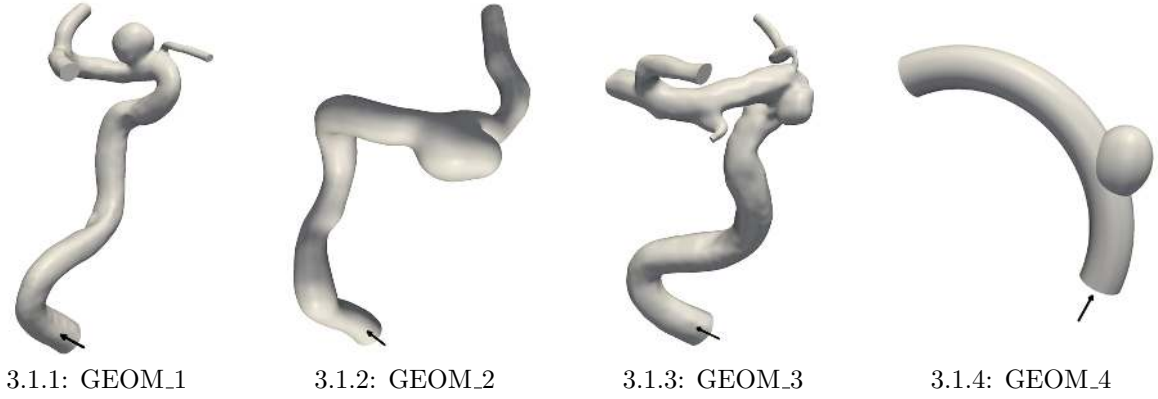|			
3.1.1: GEOM_1	3.1.2: GEOM_2	3.1.3: GEOM_3	3.1.4: GEOM_4

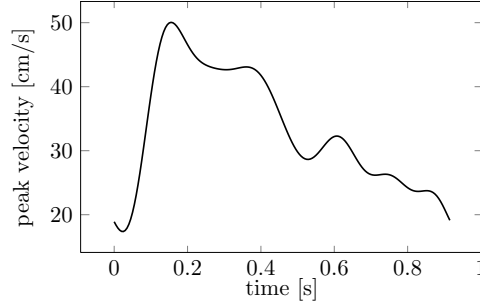Figure 3.1: Studied geometries. Black arrows denote the inflow boundary.

Figure 3.2: Archetypal waveform of the peak velocity (in units) in the internal carotid artery over one cardiac cycle, created by fitting to experimental data, from [21].

the characteristic units as well, that means the diameter of all computational arteries is approximately 0.5 of non-dimensional units.

3.2   Boundary conditions

On the boundary Γ we prescribe the following mixed boundary conditions

$$\boldsymbol{u} = \boldsymbol{0} \text{ on } \Gamma_{\text{w}}, \qquad \boldsymbol{u} = \boldsymbol{g} \text{ on } \Gamma_{\text{in}}, \qquad \boldsymbol{T}\boldsymbol{n} = \boldsymbol{0} \text{ on } \Gamma_{\text{out}}. \tag{3.2}$$

By that, we impose the wall to be non-penetrable on which the fluid perfectly adheres (no-slip), on the outflow we prescribe physical zero stress, sometimes called "do nothing" boundary condition. On the inflow boundary we prescribe either a physiological inflow condition or a constant (artificial) inflow. For both cases, the inflow is governed by a given velocity function

$$\boldsymbol{g} = \boldsymbol{g}(t, x) = g_t(t)\, \phi(t) \boldsymbol{g}_x(x). \tag{3.3}$$

12

Here $\boldsymbol{g}_x(x)$ represents a parabolic[5] profile of the inflow, $0 \leqslant |\boldsymbol{g}_x(x)| \leqslant 1$, scaled by $g_t(t)$, representing its periodic change over one cardiac cycle. Additionally, $\phi(t)$ stands for initial damping.

In arteries, the velocity profile of the blood flow is generated by the heart beat, nevertheless, the magnitude and the shape of pulses change at different parts of the arterial system, mainly due to the branching, wall deformation, and the complex curvature of the cardiovascular system. We use a profile experimentally determined for an internal carotid artery[6] by [21], see Fig. 3.2, with a period of the cardiac cycle of 0.917 s. Such a multi-harmonic function can be decomposed into Fourier series[7]

$$g_{t1}(t) = \frac{a_0}{2} + \sum_{k=1}^{7} a_k \cos(k\omega t) + b_k \sin(k\omega t), \tag{3.4}$$

where $\omega = 2\pi/T_f$ denotes the frequency of oscillation and a_k, b_k are the Fourier coefficients given by a fitting of g_t to experimental data (from [21]). As a second profile of the inflow velocity we consider a constant profile, computed as an average of the above described wave, namely

$$g_{t2}(t) = \frac{1}{T_f} \int_0^{T_f} g_{t1}(t)\, dt \approx 3.33. \tag{3.5}$$

For computational reasons we damp the wave g_t at the initial period by

$$\phi(t) = \begin{cases} \frac{1}{2}\left(1 + \cos(\pi(\frac{t}{T_f} - 1))\right) & \text{for } t < T_f, \\ 1 & \text{else,} \end{cases} \tag{3.6}$$

to obtain a smooth evolution of the flow from the initial rest state $\boldsymbol{u}(0, x) = \boldsymbol{0}$, $x \in \Omega$. Both inflow time profiles are depicted in Fig. 3.3.

3.3 Discretization

First, we discretize the system (1.7)–(1.8) in time by using a standard Crank–Nicholson method, see for instance [24], with a time stepping $\Delta t = T_f/50$ in the simulation time interval $(0, 5T_f)$. On the non-linear terms, we apply a full Newton method with a relative accuracy of $1e-8$. For the spatial discretization we use finite elements with piecewise linear and globally continuous approximations for both, the velocity and the pressure, i.e. a $\mathcal{P}_1$–$\mathcal{P}_1$ pairing. This, as a low order approximation, has an advantage in computation of large systems due to the lower number of degrees of freedom. Nevertheless, such a pairing does

---

[5]In general, the vessel cross-section may not posses a circular profile. In that case, the prescribed parabolic function needs to be properly scaled or has to have a suitable decay at the boundary of such a cross-section.

[6]Artery of our interest.

[7]For this particular case, 7 summands of the series are approximating the waveform accurately enough.
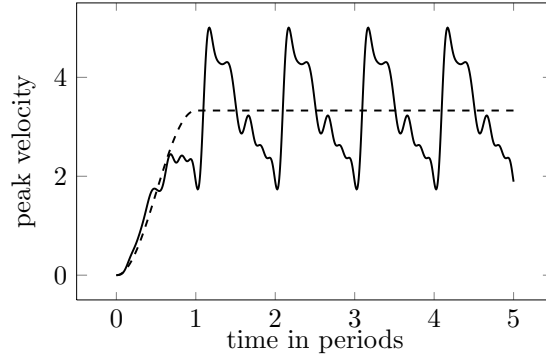
Figure 3.3: Two different inflow profiles of the function $g_t(t)$ with a scaling $\phi(t)$ from the rest state, over the computational time interval $(0, 5\,T_f)$; Full line: $g_{t_1}(t)\phi(t)$ - physiological profile, as in Fig. 3.3, dashed line: $g_{t_2}(t)\phi(t)$ - averaged (over one period) profile.

	GEOM_1	GEOM_2	GEOM_3	GEOM_4
space elements	$568,050$	$1,388,238$	$1,376,085$	$1,002,972$
dofs	$352,905$	$900,693$	$903,104$	$648,567$

Table 3.1: Numbers of spatial elements and degrees of freedom (dofs) for all considered geometries.

not satisfy the inf–sup condition, and thus, it results in an unstable method, see for instance [3]. This we overcome by the use of Bochev–Dohrmann stabilization, which is suitable for equal-order approximation, see [2]. It introduces an additional pressure penalizing term free of stabilization parameter. Moreover, it does not require a calculation of higher-order derivatives as most of other standard stabilized finite element methods.

The computations are performed on the cluster GHOST with 2 nodes, each consisting of 8 Quad-Core AMD Opteron Processors (2.3 GHz) and 256 GB RAM. The resulting linear system of equations is solved by the direct solver PARDISO, see [18]. For each geometry, the number of degrees of freedom and the number of spatial elements are presented in Tab 3.1.

4   Numerical results and discussion

As it was outlined in the introduction, we focus on the determination of the difference between the hemodynamic indicators (both AWSS and OSI) with respect to the used formula of the wall shear stress vector $\boldsymbol{\tau}_w$, see (2.5) and (2.10). This means, we aim to

4.1.1: $\textit{diff}_{\mathrm{AWSS}}$ 4.1.2: $\textit{diff}_{\mathrm{AWSS}}$ 4.1.3: $\textit{diff}_{\mathrm{AWSS}}$ 4.1.4: $\textit{diff}_{\mathrm{AWSS}}$

4.1.5: $\textit{diff}_{\mathrm{OSI}}$ 4.1.6: $\textit{diff}_{\mathrm{OSI}}$ 4.1.7: $\textit{diff}_{\mathrm{OSI}}$ 4.1.8: $\textit{diff}_{\mathrm{OSI}}$
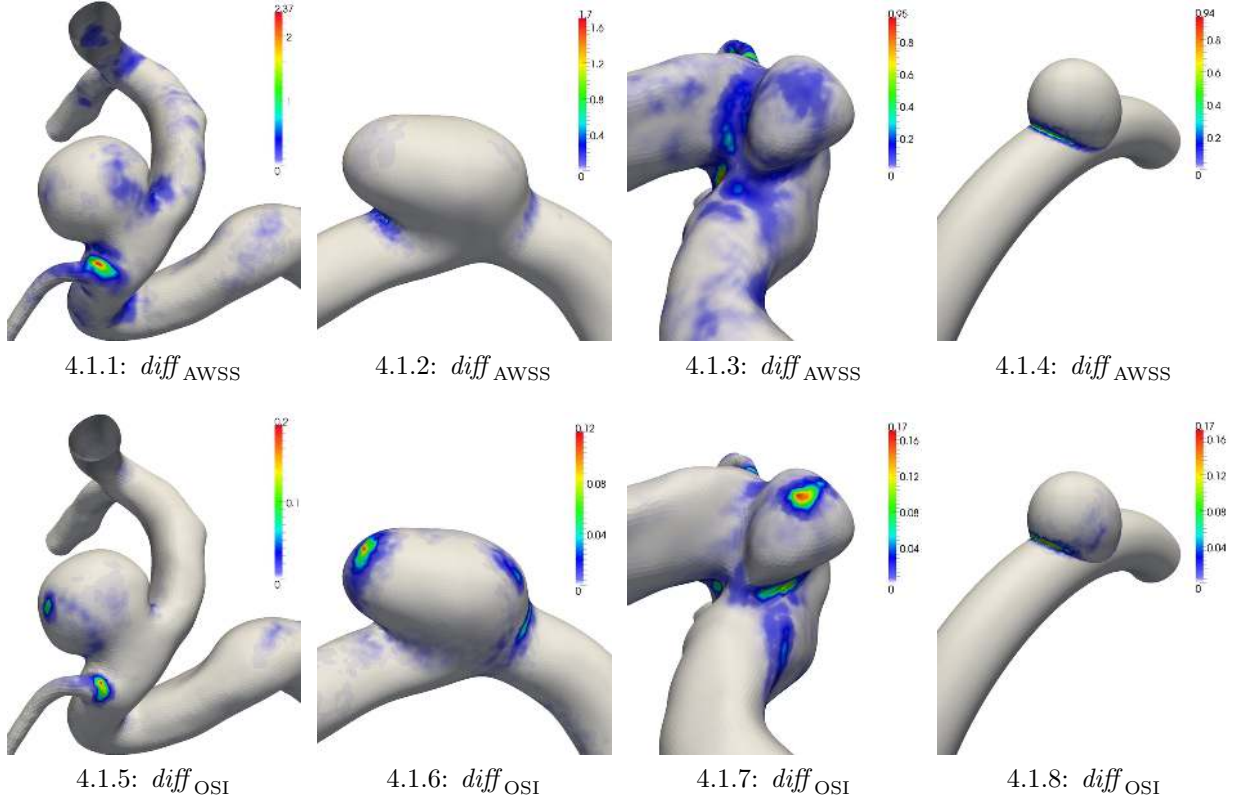
Figure 4.1: Absolute differences between AWSS and OSI computations for all four geometries. On parts of the boundary without color are the indicators identical, i.e. $\mathrm{AWSS}_1 = \mathrm{AWSS}_2$ and $\mathrm{OSI}_1 = \mathrm{OSI}_2$. Computational setting: generalized viscosity, periodic inflow.

demonstrate absolute differences

$$\textit{diff}_{\mathrm{AWSS}} := |\mathrm{AWSS}_1 - \mathrm{AWSS}_2|, \quad \text{and} \quad \textit{diff}_{\mathrm{OSI}} := |\mathrm{OSI}_1 - \mathrm{OSI}_2|, \tag{4.1}$$

for all four geometries, where AWSS_1, AWSS_2, OSI_1 and OSI_2 are defined in (2.13) and (2.15). The computational results for periodic inflow (3.4) and for the shear rate dependent viscosity model (1.4) are presented in Fig. 4.1, with zooms on the aneurysms. The results clearly show that the differences are strongly dependent on the complexity of the geometry. This correlates with the fact that near the "enough smooth" part of the boundary the characteristic of the flow is close to the simple shear. Hence, both wall shear stress vectors $\boldsymbol{\tau}_{w,1}$ and $\boldsymbol{\tau}_{w,2}$ are identical, and thus OSI and AWSS are the same for both approaches. These areas are represented in Fig. 4.1 without color. The parts of the walls where the simple shear approximation fails are either those with higher curvature (like at bifurcations, sharp curves, necks of aneurysms), or those which are near the flow vortices (like the heads of aneurysms). Even though those parts of the boundary are minor, they are exactly the critical regions where aneurysms evolve, and thus, to obtain more precise results, the whole decomposition of wall traction should be assumed.

4.2.1: AWSS$_2$ 4.2.2: *diff*$_{\text{AWSS}}$ 4.2.3: OSI$_2$ 4.2.4: *diff*$_{\text{OSI}}$

4.2.5: AWSS$_2$ 4.2.6: *diff*$_{\text{AWSS}}$ 4.2.7: OSI$_2$ 4.2.8: *diff*$_{\text{OSI}}$
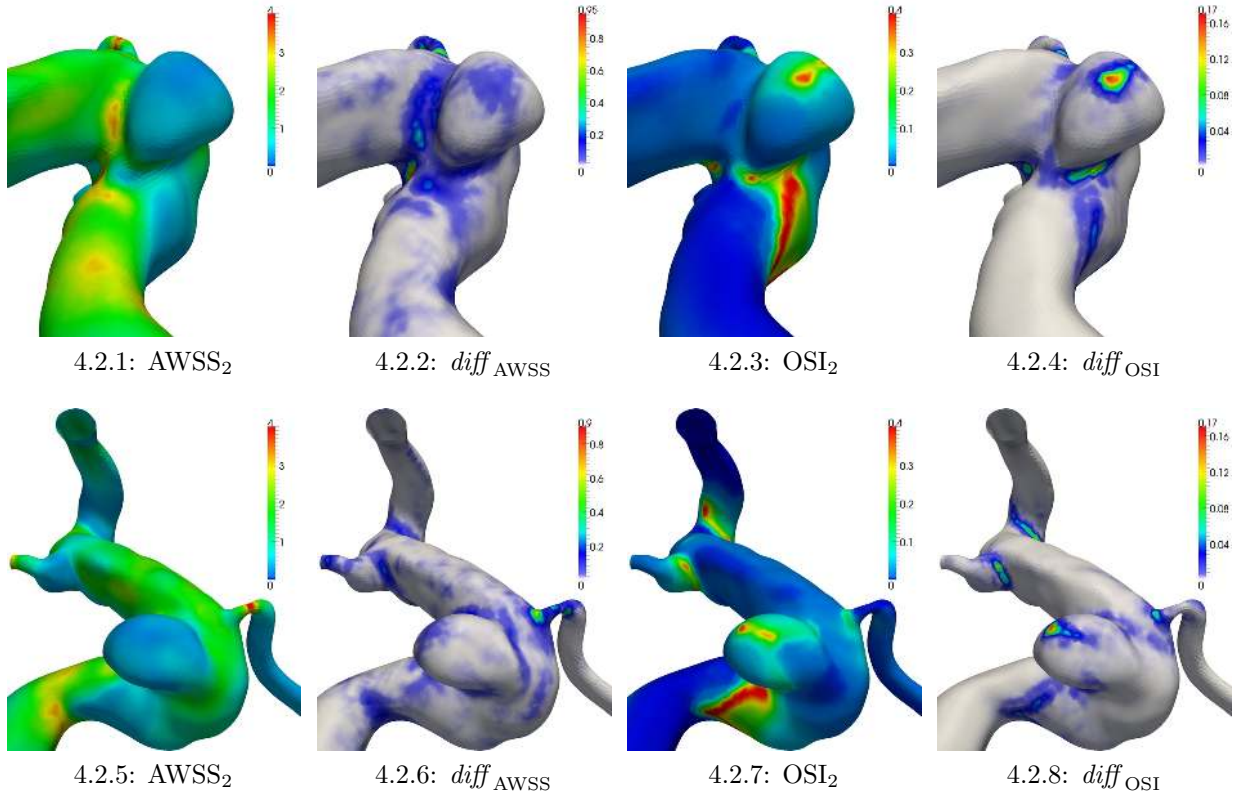
Figure 4.2: Comparison of the relative differences for third geometry in two zoomed views. For this case the maximal difference takes up to approximately 20% in AWSS and 40% in OSI with respect to the result obtained by full decomposition. Computational setting: generalized viscosity, periodic inflow.

To compare the magnitude of the differences with the actual magnitudes of computed AWSS and OSI, we include Fig. 4.2 of geometry GEOM_3. For this particular computational setting, the maximal differences are approximately of 20% in AWSS and 40% in OSI with respect to the result obtained by full decomposition. Nevertheless, the parts of the wall where the AWSS and OSI differ mostly are not identical. AWSS$_1$ differs from AWSS$_2$ mainly at the sharp curve of the main vessel, while the OSI differences are mainly located at the head of aneurysm and bifurcations. The areas where *diff*$_{\text{AWSS}}$ are highest reflect regions where vector $\boldsymbol{\tau}_w$ changes mainly in magnitude, while for the *diff*$_{\text{OSI}}$ they are determined by the $\boldsymbol{\tau}_w$ having different directions but possibly of similar magnitude during the flow period. This then causes that regions of highest AWSS/OSI differences are not always identical. For better illustration of this fact, we include line cut profiles in Fig. 4.3. For both cases, AWSS$_1$ and AWSS$_2$, respectively OSI$_1$ and OSI$_2$, exhibit similar characteristics but the values at critical regions differ. The cut 1 is represented in Fig. 4.3.1, and as it goes from front to the back, the cut parametrization in plots 4.3.2–4.3.3 goes from 0 to 1. For this cut, we observe nearly no differences in AWSS but profound differences in OSI. In the case

4.3.1: cut 1   4.3.2: AWSS along cut 1   4.3.3: OSI along cut 1

4.3.4: cut 2   4.3.5: AWSS along cut 2   4.3.6: OSI along cut 2
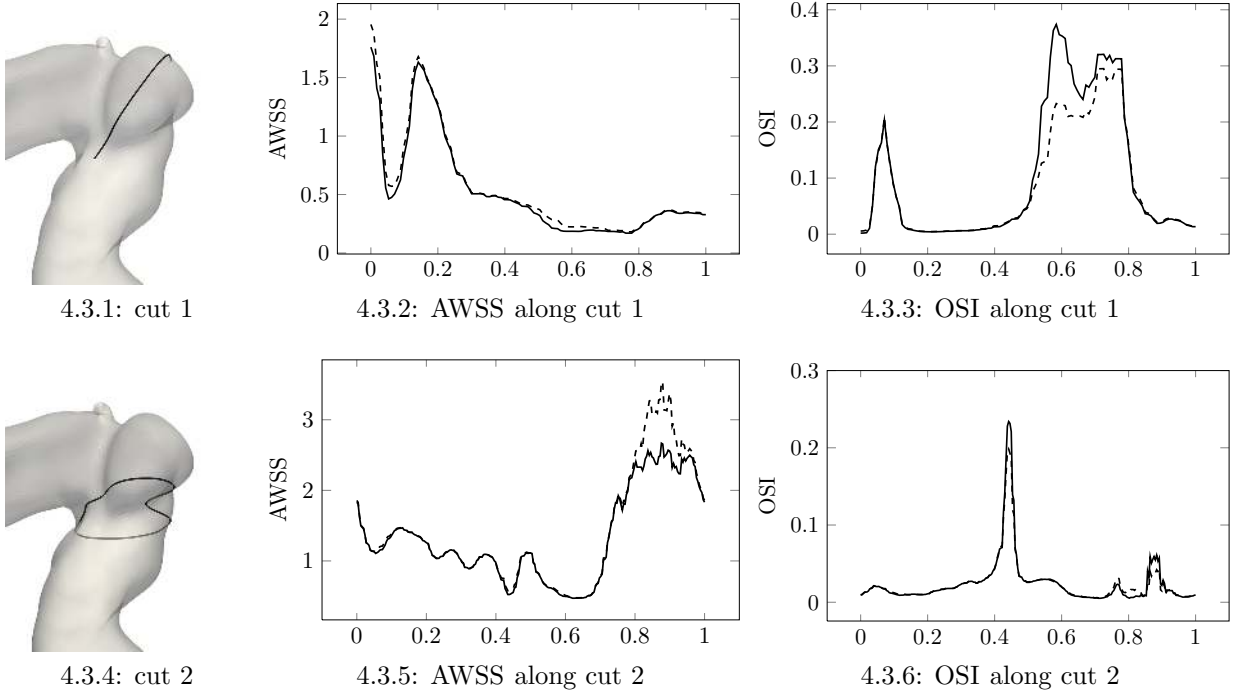
Figure 4.3: Direct comparison of the indicators on the line cuts as schematically depicted in 4.3.1 and 4.3.4. The line cut through the boundary is parametrized to the interval $(0, 1)$, used as a characterization of a position on the cut for plots in Fig. 4.3.2, 4.3.3, 4.3.5 and 4.3.6. As one can see, the differences of AWSS are placed away from the aneurysm head, while for the OSI they occur on the top of the head. Full line: full decomposition (indicators computed from $\boldsymbol{\tau}_{w,2}$), dashed line: partial decomposition (indicators computed from $\boldsymbol{\tau}_{w,1}$).

of cut 2 (Fig. 4.3.4), the remarkable differences in AWSS are positioned at the inner curve of the main vessel, i.e. the left part of the representation of cut 2. For clearer comparison reasons, the plotted values are neither smoothened nor interpolated.

As last, we present in Fig. 4.4 simulation results with focus on the influence of the computational setting on the value of OSI (here are the differences mostly distinguishable) and the corresponding differences between the full and partial decomposition approaches in computation of $\boldsymbol{\tau}_w$. The pictures in Fig. 4.4 are of geometry GEOM_2 in two mutually opposite zooms on the aneurysm head. First, we can notice remarkable influence of the used viscosity model on the OSI distribution, i.e. the difference in computation with Newtonian (constant) viscosity and generalized (shear-rate dependent) viscosity, compare first and third row of the figure. These both cases are results for periodic inflow of velocity. On the other hand, the difference between the distributions of OSI for the case of periodic and constant inflow is not of such magnitude. This is due to the fact that the flow in the aneurysm head is slowed down and it does not exhibit such a strong periodic character as in the vessel itself. Nevertheless, on the vessel wall are the characteristics much more distinguishable (partially notable in the zoom views as well). In this set of pictures, the
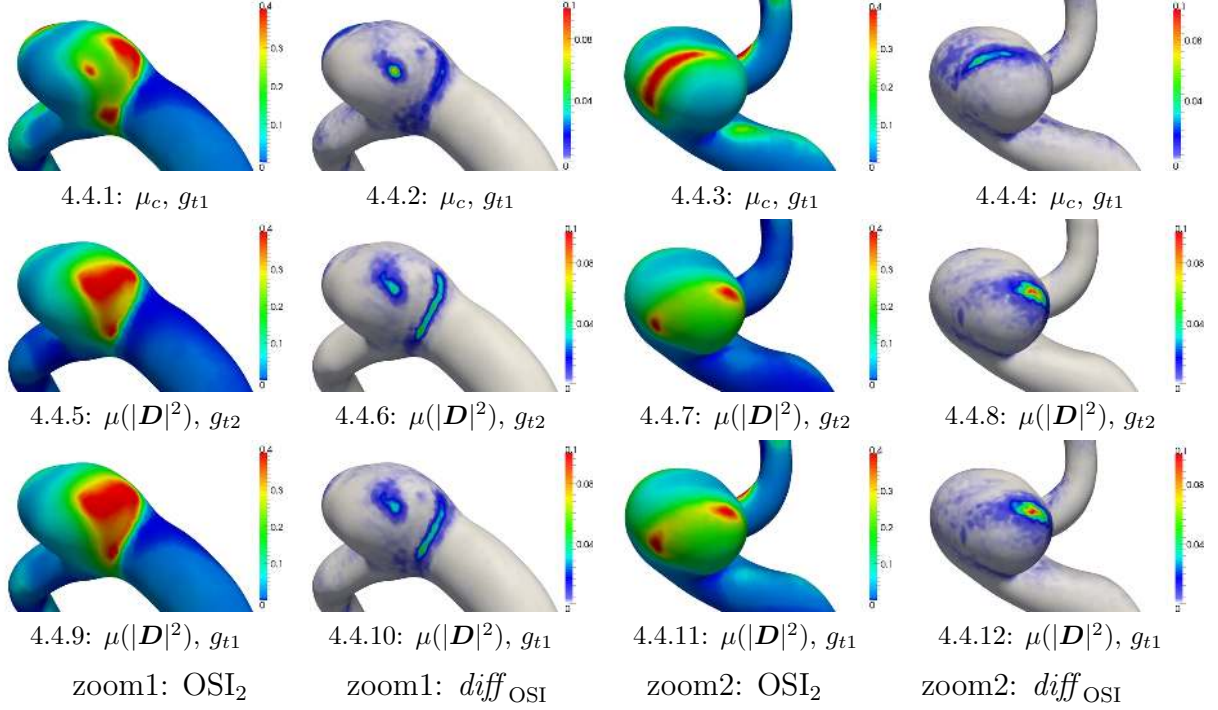
4.4.1: μ_c, g_{t1} 4.4.2: μ_c, g_{t1} 4.4.3: μ_c, g_{t1} 4.4.4: μ_c, g_{t1}

4.4.5: $\mu(|\boldsymbol{D}|^2)$, g_{t2} 4.4.6: $\mu(|\boldsymbol{D}|^2)$, g_{t2} 4.4.7: $\mu(|\boldsymbol{D}|^2)$, g_{t2} 4.4.8: $\mu(|\boldsymbol{D}|^2)$, g_{t2}

4.4.9: $\mu(|\boldsymbol{D}|^2)$, g_{t1} 4.4.10: $\mu(|\boldsymbol{D}|^2)$, g_{t1} 4.4.11: $\mu(|\boldsymbol{D}|^2)$, g_{t1} 4.4.12: $\mu(|\boldsymbol{D}|^2)$, g_{t1}

zoom1: OSI_2 zoom1: $diff_{OSI}$ zoom2: OSI_2 zoom2: $diff_{OSI}$

Figure 4.4: Comparison of OSI computed by full decomposition (from $\boldsymbol{\tau}_{w,2}$) and of the absolute differences between the two approaches, with focus on the influence of different computational setting. Top row: Newtonian model (constant viscosity), middle row: generalized Newtonian model (non-constant viscosity), constant inflow (described by function g_{t2}), bottom row: generalized Newtonian model (non-constant viscosity).

differences are defined as in (4.1).

5   Concluding remarks and outlook

This work has been focused on the illustration of the importance of the formula for wall shear stress vector in computation of hemodynamic indicators. A full decomposition approach is from our point of view a good starting point for the characterization of critical areas of artery walls with respect to the formation and progression of aneurysms. Nevertheless, in further work the models should be improved by inclusion of the most significant aspects which can influence those indicators as well. From our perspective, this includes the following. First, a more realistic blood model which can, in a reasonable range, capture the pathological behavior of blood near the critical areas and/or its non-Newtonian properties. And as a second, the influence of the wall deformation caused by the blood flow circulation. For the considered numerical method this means to include the fluid-structure interaction (FSI), and, for the modeling part, a reasonable solid-like deformation model.

Acknowledgement

References

[1] M. Anand and K. Rajagopal. A shear-thinning viscoelastic fluid model for describing the flow of blood. *International Journal of Cardiovascular Medicine and Science*, 4(2):55–68, 2004.

[2] P. Bochev and C. Dohrmann. A stabilized finite element method for the Stokes problem based on polynomial pressure projections. *International Journal for Numerical Methods in Fluids*, 46:183–201, 2004.

[3] F. Brezzi and M. Fortin. *Mixed and hybrid finite element methods*. Springer-Verlag, New York, 1991.

[4] S. Chien, S. Usami, R. J. Dellenback, M. I. Gregersen, L. B. Nanninga, and M. M. Guest. Blood Viscosity: Influence of Erythrocyte Aggregation. *Science (New York, N.Y.)*, 157:829–831, Aug. 1967.

[5] S. Chien, S. Usami, R. J. Dellenback, M. I. Gregersen, L. B. Nanninga, and M. M. Guest. Blood Viscosity: Influence of Erythrocyte Deformation. *Science (New York, N.Y.)*, 157:827–829, Aug. 1967.

[6] K. S. Cunningham and A. I. Gotlieb. The role of shear stress in the pathogenesis of atherosclerosis. *Laboratory investigation*, 85(1):9–23, Jan. 2005.

[7] G. Galdi, R. Rannacher, A. Robertson, and S. Turek. *Hemodynamical flows: modeling, analysis and simulation*, volume 37. Birkhäuser, Basel, Boston, Berlin, 2008.

[8] A. Gambaruto, J. a. Janela, A. Moura, and A. Sequeira. Sensitivity of hemodynamics in a patient specific cerebral aneurysm to vascular geometry and blood rheology. *Mathematical Biosciences and Engineering*, 8(2):409–423, Apr. 2011.

[9] R. J. Guzman, K. Abe, and C. K. Zarins. Flow-induced arterial enlargement is inhibited by suppression of nitric oxide synthase activity in vivo. *Surgery*, 122(2):273–280, Aug. 1997.

[10] F. Hazama, H. Kataoka, E. Yamada, K. Kayembe, N. Hashimoto, M. Kojima, and K. Chiegon. Early changes of experimentally induced cerebral aneurysms in rats. Light-microscopic study. *The American journal of Pathology*, 124:399–404, 1986.

[11] K. N. Kayembe, M. Sasahara, and F. Hazama. Cerebral aneurysms and variations in the circle of Willis. *Stroke*, 15(5):846–850, Sept. 1984.

[12] D. N. Ku. Blood Flow in Arteries. *Annual Review of Fluid Mechanics*, 29(1):399–434, Jan. 1997.

[13] D. N. Ku, D. P. Giddens, C. K. Zarins, and S. Glagov. Pulsatile flow and atherosclerosis in the human carotid bifurcation. Positive correlation between plaque location and low oscillating shear stress. *Arteriosclerosis, Thrombosis, and Vascular Biology*, 5(3):293–302, May 1985.

[14] A. Malek, S. Alper, and S. Izumo. Hemodynamic shear stress and its role in atherosclerosis. *The Journal of the American Medical Association*, 282(21):2035–2042, 1999.

[15] J. Málek, J. Nečas, and M. Růžička. On the non-Newtonian incompressible fluids. *Mathematical models and methods in applied sciences*, 3(1):35–63, 1993.

[16] S. Ramalho and A. Moura. Sensitivity to outflow boundary conditions and level of geometry description for a cerebral aneurysm. *International Journal for Numerical Methods in Biomedical Engineering*, 28:697–713, 2012.

[17] H. Samady, P. Eshtehardi, M. C. McDaniel, J. Suo, S. S. Dhawan, C. Maynard, L. H. Timmins, A. a. Quyyumi, and D. P. Giddens. Coronary artery wall shear stress is associated with progression and transformation of atherosclerotic plaque and arterial remodeling in patients with coronary artery disease. *Circulation*, 124(7):779–88, Aug. 2011.

[18] O. Schenk, M. Bollhöfer, and R. Römer. On large scale diagonalization techniques for the Anderson model of localization. *SIAM Rev.*, 50(1):91–112, 2008.

[19] D. Sforza, C. Putman, and J. Cebral. Hemodynamics of cerebral aneurysms. *Annual review of fluid mechanics*, 41:91–107, 2009.

[20] J. V. Soulis, G. D. Giannoglou, Y. S. Chatzizisis, K. V. Seralidou, G. E. Parcharidis, and G. E. Louridas. Non-Newtonian models for molecular viscosity and wall shear stress in a 3D reconstructed human left coronary artery. *Medical engineering & physics*, 30(1):9–19, Jan. 2008.

[21] M. Thiriet. *Biology and Mechanics of Blood Flows.* Springer New York, New York, NY, 2008.

[22] G. Thurston. Viscoelasticity of human blood. *Biophysical Journal*, 12(4):1205–1217, 1972.

[23] G. Thurston. Rheological parameters for the viscosity viscoelasticity and thixotropy of blood. *Biorheology*, 16(3):149–162, 1979.

[24] S. Turek, L. Rivkind, J. Hron, and R. Glowinski. Numerical Study of a Modified Time-Stepping θ-Scheme for Incompressible Flow Simulations. *Journal of Scientific Computing*, 28(2-3):533–547, Mar. 2006.

[25] S. M. Wasserman and J. N. Topper. Adaptation of the endothelium to fluid flow: in vitro analyses of gene expression and in vivo implications. *Vascular Medicine*, 9(1):35–45, Feb. 2004.

[26] K. Yeleswarapu, M. Kameneva, and K. Rajagopal. The flow of blood in tubes: theory and experiment. *Mechanics Research*, 25(3):257–262, 1998.

Erschienene Preprints ab Nummer 2012/1

2010/1   G. Of, T. X. Phan, O. Steinbach: Boundary element methods for Dirichlet boundary control problems.

2010/2   P. D. Ledger, S. Zaglmayr: hp–Finite element simulation of three–dimensional eddy current problems on multiply connected domains.

2010/4   S. Engleder, O. Steinbach: Boundary integral formulations for the forward problem in magnetic induction tomography.

2010/5   Z. Andjelic, G. Of, O. Steinbach, P. Urthaler: Direct and indirect boundary element methods for magnetostatic field problems.

2010/8   A. Klawonn, U. Langer, L. F. Pavarino, O. Steinbach, O. B. Widlund (eds.): Workshop on Domain Decomposition Solvers for Heterogeneous Field Problems, Book of Abstracts.

2010/9   O. Steinbach, G. Unger: Convergence analysis of a Galerkin boundary element method for the Dirichlet Laplacian eigenvalue problem.

2010/10   O. Steinbach (ed.): Workshop on Computational Electromagnetics, Book of Abstracts.

2010/11   S. Beuchler, V. Pillwein, S. Zaglmayr: Sparsity optimized high order finite element functions for H(div) on simplices.

2010/12   U. Langer, O. Steinbach, W. L. Wendland (eds.): 8th Workshop on Fast Boundary Element Methods in Industrial Applications, Book of Abstracts.

2011/1   O. Steinbach, G. Unger: Convergence orders of iterative methods for nonlinear eigenvalue problems.

2011/2   M. Neumüller, O. Steinbach: A flexible space–time discontinuous Galerkin method for parabolic initial boundary value problems.

2011/3   G. Of, G. J. Rodin, O. Steinbach, M. Taus: Coupling methods for interior penalty discontinuous Galerkin finite element methods and boundary element methods.

2011/4   U. Langer, O. Steinbach, W. L. Wendland (eds.): 9th Workshop on Fast Boundary Element Methods in Industrial Applications, Book of Abstracts.

2011/5   A. Klawonn, O. Steinbach: Söllerhaus Workshop on Domain Decomposition Methods, Book of Abstracts

2011/6   G. Of, O. Steinbach: Is the one-equation coupling of finite and boundary element methods always stable?

2012/1   G. Of, O. Steinbach: On the ellipticity of coupled finite element and one-equation boundary element methods for boundary value problems.

2012/2   O. Steinbach: Boundary element methods in linear elasticity: Can we avoid the symmetric formulation?

2012/3   W. Lemster, G. Lube, G. Of, O. Steinbach: Analysis of a kinematic dynamo model with FEM-BEM coupling.

2012/4   O. Steinbach: Boundary element methods for variational inequalities.

2012/5   G. Of, T. X. Phan, O. Steinbach: An energy space finite element approach for elliptic Dirichlet boundary control problems.

2012/6   O. Steinbach, L. Tchoualag: Circulant matrices and FFT methods for the fast evaluation of Newton potentials in BEM.

2012/7   M. Karkulik, G. Of, D. Praetorius: Convergence of adaptive 3D BEM for weakly singular integral equations based on isotropic mesh-refinement.

2012/8	M. Bulicek, P. Pustejovska: On Existence analysis of steady flows of generalized Newtonian fluids with concentration dependent power–law index.
2012/9	U. Langer, O. Steinbach, W. L. Wendland (eds.): 10. Workshop on Fast Boundary Element Methods in Industrial Applications. Book of Abstracts.
2012/10	O. Steinbach: Boundary integral equations for Helmholtz boundary value and transmission problems.
2012/11	A. Kimeswenger, O. Steinbach, G. Unger: Coupled finite and boundary element methods for vibro–acoustic interface problems.
2012/12	T. X. Phan, O. Steinbach: Boundary element methods for parabolic boundary control problems.
2013/1	L. John, P. Pustejovska, O. Steinbach: On hemodynamic indicators related to aneurysm blood flow.
2013/2	G. Of, O. Steinbach (eds.): 9th Austrian Numerical Analysis Day. Book of Abstracts.
2013/3	D. Amann, A. Blaszczyk, G. Of, O. Steinbach: Simulation of Floating Potentials in Industrial Applications by Boundary Element Methods.
2013/4	L. John, O. Steinbach: Schur complement preconditioners for the biharmonic Dirichlet boundary value problem.
2013/5	J. Hron, P. Pustejovska: Comparison of stabilized finite element methods for simulation of flow of diluted polymeric liquids